Chemistry and Materials

The Center for Science Innovation

Research Article

*Chem. Mater. 5 (2) 2026, 85-94*

# Theoretical Evidence for the Antibacterial and Antioxidant Potentials of a New Molybdenum Tricarbonyl Complex

**Tenimu Adogah Abubakar[1,]*, Abdulakeem Busari[2], Jude Ehwevwerhere Emurotu[1], Dele Peter Fapojuwo[3], Oluwagbemiga T. Amusan[4], Uche Basil Eke[1,4]**

[1]Chemistry Department, Faculty of Physical Sciences, Federal University Lokoja PMB 1154, Lokoja, Nigeria
[2]Department of Chemistry, Faculty of Natural and Applied Sciences, Sule Lamido University, Kafin Hausa. P.M.B. 048, Jigawa state
[3]Department of Chemistry, Nelson Mandela University, PO Box 77000, Gqeberha 6031, South Africa
[4]Department of Chemistry, Faculty of Science, University of Ilorin, P.M.B. 1515, Kwara State
*Corresponding author: ubeke@unilorin.edu.ng

**Received**
23 April 2026
**Received in revised form**
03 June 2026
**Accepted**
12 June 2026

**DOI**
https://doi.org/10.56425/cma.v5i2.140

## Abstract

The development of low energy light-activated therapeutics with precise targets is currently receiving pronounced attention. Here we report the evaluation of a novel mer-tricarbonylmolybdenum(0) complex with benzyl isonicotinoyl hydrazone (BIH) as ancillary ligands. The complex is a photoactive carbon monoxide-releasing molecule (PhotoCORM) with dual action. Spectroscopic characterization (IR, NMR) and the elemental analysis results confirmed a meridional octahedral geometry tricarbonyl complex with a para substitution pattern for the coordinating pyridinic nitrogen atom of the ancillary ligand. FTIR spectral analysis strongly suggested that the para substitution mode of the ligand attenuated metal-to-ligand π-backbonding, resulting in the weakening of the Mo-C bond. Time-dependent density functional theory (TD-DFT) calculations showed that a highly allowed Metal-to-Ligand Charge Transfer (MLCT) in the visible light region ($\lambda_{max}$ = 587.45 nm) initiated the photolysis process. Experimental evidence supported that upon irradiation, the complex undergoes dissociation at a rapid rate ($k = 9.7x10^{-2}\ s^{-1}$). Released CO is successfully delivered to biological heme sites as confirmed by carbonmonoxy myoglobin (MbCO) formation. *In silico* molecular docking simulation with SwissDock program demonstrated that possible release of hydrazone ancillary ligand may effectively target the active site of keap1 (PDB: 4L7B) and those of essential bacterial proteins; LasR (PDB: 3IX3), MRSA PBP2a (PDB:5M18) and *E. coli* DNA Gyrase (PDB: 6F86). *In vitro* antibacterial assay carried out to validate the theoretical broad-spectrum activity of the ligand, and the CO poisoning of the heme indicates significant growth inhibition against *S aureus, E. coli, and P. aeruginosa* in a dose-dependent manner. These results highly suggest this novel photoCORM as a promising synergistic antimicrobial agent.

***Keywords:*** photoCORM, TD-DFT, molybdenum tricarbonyl, molecular docking, CORM antibacterial

## 1. Introduction

Substituted transition metal carbonyls are recognized as the best class of carbon monoxide releasing molecules (CORMs). With carefully selected metal and biologically active ancillary ligands they display better antibacterial activity compared to the homonuclear starting complex [1]. We have previously reported the antibacterial activities of tungsten and molybdenum tricarbonyls designed with hydrazones as ancillary ligand [2,3]. They showed remarkable activity against Gram-positive and Gram-negative pathogens. Mechanistic studies implicate CO release by CORMs in physiological conditions as a trigger for antibacterial action. Such CO released by

CORMs is suspected to impair bacterial respiratory pathway as the major cause of antibacterial action [4].

Several CORMs have been reported to have impressive antibacterial activities [5]. Although the mechanisms of CORMs' antibacterial action are not entirely understood, it is thought to include disruption of bacterial membranes, possibly due to hydroxy radical production, interference with metal ion uptake in bacteria, and CO binding to respiratory cytochromes, which may hinder bacterial respiration [1]. Major challenges in achieving useful antibacterial CORMs include tissue-specific CO delivery and toxicity, as CORMs can be toxic at higher doses [6]. There is therefore a need to devise strategies for optimizing carbon monoxide release from CORMs. This can be achieved by a careful selection of tunable ancillary ligands, metal centre of desirable redox potential, stability, and biocompatibility.

CORMs have elicited burgeoning scientific interest and some debates. A recent investigation reported that water-soluble CORM-2, which is a potential antibacterial agent, kills bacteria both in culture and animal models but is benign towards mammalian cells [7]. According to the researchers, CORM-2 releases less than 0.1 M CO per mol, which is negligible, and this challenges the prevailing notion that CO is responsible for the antibacterial activity of the CORM. Ruthenium accumulation is fingered for its antibacterial activity and not CO release.

Theoretical computational chemistry promises a pivotal role in advancing our understanding of the properties, bioactivity, and mechanism of CORMs. However, this application is currently underexplored. We can gain insight into CORMs’ CO release kinetics and estimate CO liberation rates with knowledge of the thermodynamics and reaction pathway parameters [8,9]. Quantum mechanical optimization and frequency calculations can be very valuable in the design of CORMs as a computational tool in predicting stability, reactivity, CO release, and binding affinities. Density functional theory (DFT) has been used to elucidate metal-CO bonding, giving insights into metal carbonyl complexes [10]. Computation models and docking studies with pathogens are reported to provide information regarding toxicity and antibacterial targets. DFT calculations performed using the B3LYP/LANL2DZ basis set were used to explore the CO release capacity of some manganese-containing CORMs [11,12]. The calculations predicted the Mn-CO bond dissociation energies, providing insight into the amount of CO released by the CORMs. The natural bond orbital (NBO) analysis revealed the donor-acceptor interactions and bond stabilization energies of Mn-CO within the CORMs studied. Impressively, the study analyzed the nucleophilic attack of putative ligands at the metal vacant site using ligand-exchange reaction energies. Calculated second dissociation energies provided insights into the observed stoichiometry [8,13]. Similar DFT studies of some group 7 CORMs bearing pyridine-based moieties as ancillary ligand compared the electronic properties of manganese and rhenium tricarbonyl complexes in terms of their carbon monoxide (CO) releasing tendency. Calculated absorbance, energy gap, and metal-to-ligand charge transfer (MLCT) percentage were employed in characterizing the tendency of the tricarbonyl complexes in labilization of CO [14].

Both experimental and theoretical analyses have been used to study Mn PhotoCORMs; Mn(I) tricarbonyl complexes containing the di(2-picolyl)amine and similar units with various electron-withdrawing ligands. DFT calculations and TD-DFT reveal their CO-releasing potential [12,13,15]. Electronic transition calculations reveal a robust MLCT, which weakens the metal-CO back bonding and facilitates rapid CO release. Similarly, TD-DFT calculations using both BP86 and B3LYP functionals were employed to study electronic properties, molecular orbitals, and excitation energies. These reveal information about the electronic structure and CO-releasing behavior of the complexes [16]. Molecular docking studies have proved to be useful in the investigation of CO-releasing coumarin derivatives as an antitumor agent. However, photoCORM research is currently challenged with issues of light activation wavelength and tissue penetration, aqueous stability, toxicity of central metal atom, targeted delivery etc.

In the current study, we have employed a novel approach of using computational chemistry to get theoretical insights into the structure, reactivity, CO release mechanism, antioxidant, and antibacterial action of a tricarbonyl molybdenum(0) containing benzylisonicotinoyl hydrazone as an ancillary ligand. This can assist in the elucidation of the exact mechanism of antibacterial action. The choice of the Mo(0) tricarbonyl, a d6 species for this study, is intended to address issues of biocompatibility, favourable light activation and kinetic control. The tricarbonyl core can improve CO release lability compared to lower di- and mono-carbonyls. This scaffold if conjugated to an extended π-conjugating system such as the isonicotinoyl hydrazone ancillary ligand will likely improve light activation and CO lability.

## 2. Materials and Method

### 2.1. Materials

Molybdenum hexacarbonyl, trimethylamine N-oxide dihydrate (TMNO), isonicotinic hydrazide (INH), benzaldehyde, tetrahydrofuran (THF), acetonitrile, and dichloromethane were purchased from Sigma Aldrich and used without further purification. All other reagents used in this work were all-purpose laboratory reagents. All reactions involving metal carbonyls were performed under pure dry nitrogen gas using manipulated Schlenk techniques. Solvents were of reagent grade and purified according to standard methods.

### 2.2. Preparation of (E)-N'-benzylideneisonicotinoyl hydrazide (BIH)

The ligand synthesis follows the protocol method reported for the condensation reaction between hydrazides and aldehydes to yield asymmetric Schiff base hydrazone [3]. Isonicotinic acid hydrazide (1.827 g; 0.013 mol) dissolved in ethanol in a round-bottom flask was added benzaldehyde (1.413 g; 0.013 mol) with constant stirring. The mixture was refluxed for 4 h, and the product was collected in a beaker, which crystallized immediately on cooling. The white solid obtained by filtration was recrystallized from ethanol and dried over fused calcium chloride in a desiccator and then weighed (Yield = 73%).

### 2.3. Preparation of $[Mo(CO)_3(BIH)_3]$

In a one-pot synthesis, a mixture of $Mo(CO)_6$ (0.396 g; 1.43 mmol), BIH (1.014 g; 4.53 mmol) previously dissolved in 10 mL of methanol and trimethylamine N-oxide dihydrate (0.339 g; 3.05 mmol) in 25 mL of tetrahydrofuran was stirred under dinitrogen at ambient temperature. An initial yellow solution changed to orange and finally to a reddish-brown suspension. The reaction was allowed to stand for 36 h, and the mother liquor was reduced to a small volume under reduced pressure. The reddish-brown solid was isolated by vacuum filtration and washed with a hexane-dichloromethane mixture and dried over silica gel in a desiccator [17].

### 2.4. Characterizations

Infrared and Raman spectra were obtained using a SHIMADZU Fourier transform infrared spectrometer using the KBr disc pellets technique and ProRaman-L-785B Raman analyzer, respectively. NMR spectra were recorded using a Bruker NMR-400 MHz spectrometer. UV-1800 Series spectrophotometer configured with a slit width of 1.0 nm and a light source change wavelength of 560 nm was used to record absorbance spectra data.

### 2.5. Computational Studies

The 2D guess structures of the compounds were drawn in ChemDraw and uploaded to the GaussView16 interface. The optimization and frequency calculations of the clean structures were carried out using the DFT, TD-DFT methods, and B3LYP/6-311+G (d,p) model chemistry in Gaussian09 [18]. The online programs SwissADME [19] and pkCSM [20] were used for the ADMET profiling of the ligands. The molecular docking studies to examine the interactions between the organic ligands against LasR quorum-sensing receptor of P. aeruginosa (PDB:3IX3), PBP2a transpeptidase of MRSA (PDB: 5M18), and the DNA Gyrase B subunit of E. Coli (PDB: 6F86) [21] and Keap1 4L7B [22] were carried out using the SwissDock program [23], [24]. The 3D structure of the P. aeruginosa (PDB:3IX3), MRSA (PDB: 5M18), PDB: 6F86, and PDB: 4L7B were downloaded from the RCSB Protein Databank. The docking results were analyzed using ChimeraX [25,26] and BIOVIA Discovery Studio Analyzer software [27].

### 2.6. Kinetics of CO Release by Metal Carbonyl Complexes

The substituted molybdenum tricarbonyl (0.005 g) placed in a quartz cuvette, was added to 1.00 mL DMSO solution. The mixture was shaken to ensure complete dissolution of the metal carbonyl, and the absorbance was immediately recorded to determine the λmax. Fresh solutions were then prepared, and absorbance was recorded at the $\lambda_{max}$ observed for the complex to determine the rates of CO release. Graphical plots of absorbance versus time were obtained. The apparent rate of CO release was calculated from the ln[C] versus time plot for the substituted tricarbonyl complex.

### 2.7. CO Delivery to Myoglobin in Solution [28]

Equine heart myoglobin (53 µM) was dissolved in phosphate-buffered saline (pH 7.4), constituted by dissolving one buffer tablet in 200 mL of deionized water. The solution was reduced by adding sodium dithionite. The concentration of deoxy-myoglobin (deoxy-Mb) generated was calculated to determine the concentration of tricarbonyl added. The initial absorbance was recorded immediately on adding the tricarbonyl complex. For Carbonmonoxy myoglobin (Mb-CO) formation, the cuvette was irradiated using a monochromatic LED light source with maximum centered at 560 nm. The light intensity was maintained at 20 $mW/cm^2$ and the spectra was monitored over time at regular intervals.

### 2.8. Antibacterial Studies of Substituted Molybdenum Tricarbonyl carbonyl

Test Microorganisms - The *Staphylococcus aureus, Escherichia coli, and Pseudomonas aeruginosa* clinical bacterial isolates, used for this study, were collected from the Culture Collection Center, Center for Vaccine and Drug Development STEP-B, Federal University of Technology, Minna, Nigeria.

Preliminary screening, Minimum inhibitory concentration (MIC) and Minimum Bactericidal Concentration (MBC) of the substituted metal carbonyl complex were determined as described in the literature [17]. The synthesized carbonyls were screened for antibacterial activity in comparison with 70 µM/mL standard antibiotic (Amoxicillin). The deliberate choice of amoxicillin is to serve as comparative control, specifically due to its known resistance to *P. aeruginosa* and *S. aureus*. The screening was done using the agar well diffusion method. The test compounds were reconstituted using DMSO at varied concentrations (2 mM - 250µM). Exactly 20 mL of sterilized nutrient agar was dispensed into each of 12 sterile petri dishes. The agar was allowed to set, inoculated, and in each of the plates, 5 mm wells were bored on each of the plates using a sterile cork-borer. Thereafter, the wells were filled with 160 µL of varied concentration (2 mM, 1 mM, 500 µM, 250 µM and 150 µM) of samples using a microtiter-pipette. This was allowed to diffuse at room temperature for two hours. The plates were incubated at 37 ºC for 24 h aerobically. The sample solution was used as a control.

**Table 1.** Selected FTIR/Raman Diagnostic bands.

| Group | IR Frequency ($cm^{-1}$) |  | Raman shift ($cm^{-1}$) |
|---|---|---|---|
|  | Experimental | Calculated |  |
| N-H | 3204, 3063 | 3548 | - |
| Terminal CO | 1743, 1909, 2071 | 1884, 1864, 2007 | 1790, 2050, 2054 |
| Ar C=H, C=N | 1565, 1491 | 1685 | - |
| Amide I | 1653 | 1751 | - |
| Amide II | 1565, 1144, 1128 | 1557 | - |
| M-CO | 590 | 547, 387 | 546 |
| M-N | 942 | 454 | 857 |
| M-C | 426 | 415 | 409 |

Positive test results were recorded when a zone of inhibition was observed after 24 h of incubation. For the MIC and MBC serial dilution of the carbonyl solution was done using 2 mL of nutrient broth in six (6) test tubes to obtain varied concentration (2 mM/mL, 1 mM/mL, 500 µM/mL, 250 µM/mL, 125 µM/mL and 62.5 µM/mL). The tubes were inoculated with 0.2 mL of standardized inocula of the bacterial isolates. The tubes were incubated overnight at 37ºC. Growth of the culture was examined by visual observation. Culture tube with the lowest concentration of the metal carbonyl which exhibited no growth was considered as the MIC value and the tube lacking turbidity was re-inoculated in fresh medium to obtain the MBC value. The minimal concentration of the sample that inhibited the growth of bacterial cells upon re-inoculation in Muller-Hinton agar was considered as MBC value.

## 3. Results and Discussion

### 3.1. Spectroscopic Characterization and Electronic Properties

The experimental FTIR/Raman and 1H NMR spectra of the tricarbonyl complexes are presented in Table 1 and Fig. 1, respectively.

The theoretical FTIR data are presented alongside the experimental values. The bands appearing at 1743, 1909, and 2071 cm-1 in the FTIR spectrum are assigned stretching CO vibrations. These bands are diagnostic of the extent of Metal-to-ligand π-backbonding [28]. The CO ligand positioned directly opposite an ancillary ligand is electron withdrawing as it is conjugated directly with the coordinating pyridine N via resonance. The CO significantly pulls electron density away from the N, making it electron-deficient and a weaker σ-donor to the Mo centre.

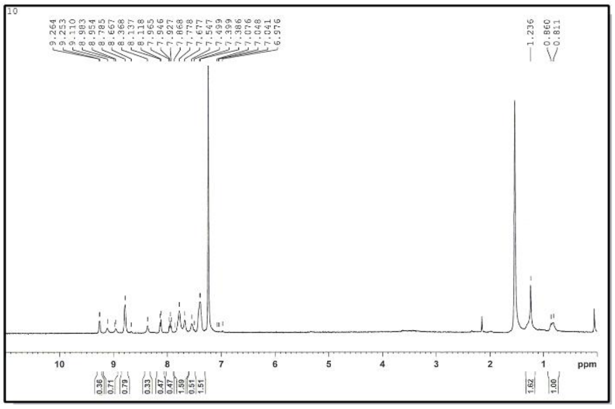

**Figure 1**. 1H NMR spectrum of the substituted tricarbonyl.

The 1H NMR spectroscopy perfectly corroborates the FTIR result; the tricarbonyl complex displayed a relatively symmetrical splitting pattern in the aromatic region (7.0-8.8 ppm). This non-clustered splitting is characteristic of a 1,4-disubstituted (para)pyridine ring displaying two distinct doublets for the four pyridine protons. The CHN elemental analysis (Table 2) and the 1H NMR and vibrational spectroscopic data all indicated a meridional tricarbonyl complex with the proposed structure (Fig. 2).

**Table 2.** Theoretical and experimental values of the percentage of C, H, and N in the complexes.

| Compounds | Molecular mass | C | | H | | N | |
|---|---|---|---|---|---|---|---|
| | | Calc. | Found | Calc. | Found | Calc | Found |
| $Mo(BIH)_3(CO)_3$ ($C_{42}H_{33}N_9O_6Mo$) | 855.73 | 58.95 | 58.46 | 3.89 | 4.01 | 14.73 | 14.40 |

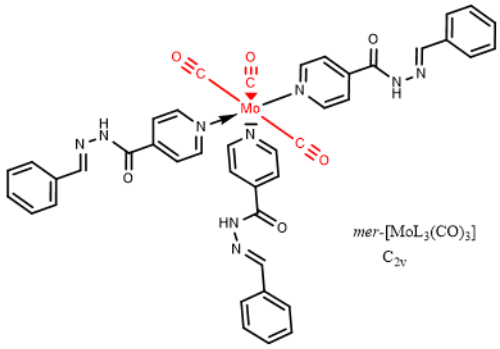

**Figure 2.** The proposed structure of the tricarbonyl complex.

The geometry and electronic distribution in the molecule, according to the spectral analysis, affect the strength of the Mo-C bond. The rate of CO dissociation in metal carbonyls is largely determined by this M-C bond. According to the FTIR analysis, this para-substituted hydrazone is a weaker electron donor due to the resonance effect of the para electron-withdrawing substituent. This depletes electron density, leading to weaker π-backbonding (Mo→CO). This leaves the Mo-C inherently weaker and more labile, and the thermal or photochemical cleavage required to release the CO will occur more readily and at a faster rate [20].

### 3.2. Optimized Structure, Global Reactivity Parameters, and Molecular Electrostatic Potential (MEP) Map

The MEP map and global reactivity parameters calculated from the optimized ground state geometry can help in the understanding of the chemical behaviour and molecular interaction profile of the studied tricarbonyl. The MEP map (Fig. 3) revealed that the oxygen atom of the CO coordinated to the Mo atom, and the amide carbonyl of the hydrazone ligand is in highly nucleophilic regions. While in the electrophilic region is centred over the aromatic protons and the N-H of the ligand. This charge polarization suggests the tricarbonyl possesses adequate physiological solubility.

The chemical hardness and chemical potential calculated from the HOMO-LUMO values (Table 3) indicate a moderately soft and highly polarizable system. This electronic softness enhances the large instantaneous shift in electron density required during the MLCT to trigger CO release. The electrophilicity index of 4.89 eV suggests a strong propensity for the carbonyl to act as an electron acceptor during initial biological interaction before photolysis.

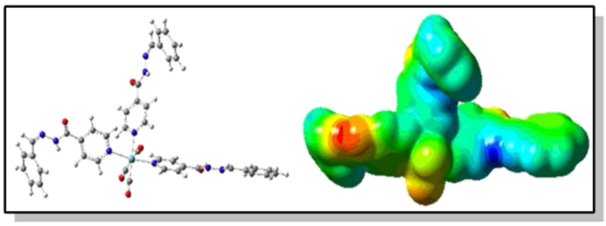

**Figure 3.** Optimized structure and Molecular Electrostatic Potential Map of the substituted tricarbonyl complex.

### 3.3. Frontier Molecular Orbital (FMO) Analysis

The spatial distribution and energy of molecular orbitals (Fig. 4) can also provide useful insight into the application of the studied tricarbonyl as a photoactivatable CORM. The calculated energy gap of 2.239 eV is narrow and corresponds to an electronic transition in the visible region ($\lambda_{max}$ = 554 nm), which is suitable for biological applications and can allow for deeper tissue penetration with minimal phototoxicity. This is in substantial agreement with the TD-DFT findings, further suggesting the carbonyl's preference to target visible light excitation. The spatial distribution of the frontier orbitals provides mechanistic information regarding photo-induced CO release. The HOMO electron density is heavily localized in the mer-[$Mo(CO)_3$] moiety, revealing the dπ-π* metal-to-ligand backbonding that stabilizes the tricarbonyl. But the LUMO is localized

**Table 3.** Global reactivity Parameter of mer-Mo $(CO)_3(BIH)_3$.

| | HOMO | LUMO | ΔE | μ | η | ω |
|---|---|---|---|---|---|---|
| $Mo(BIH)_3(CO)_3$ | -4.4278 | -2.1894 | 2.2384 | -3.3086 | 1.1192 | 4.890 |

almost exclusively on the extended conjugated π-system of the isoniazid hydrazone ancillary ligand in the para position. These electronic events accompanying the lowest-energy excitation constitute a pronounced Metal-to-Ligand Charge Transfer (MLCT), suggesting that upon absorption of a photon by the molecule, electron density is acutely depleted from the Mo centre and transferred to the peripheral hydrazone ligand. The metal core undergoing a transient oxidation leads to a weakening of the M-CO π-backbonding, which kinetically labilizes the Mo-C bond, resulting in controlled release of CO.

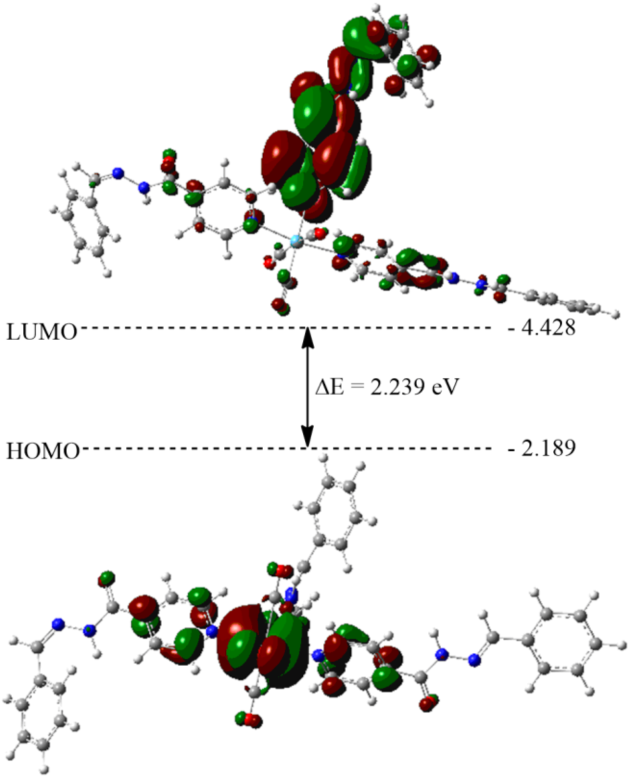

**Figure 4.** Frontier Molecular Orbitals displaying electron distribution and energy change.

### 3.4. Time-Dependent Density Functional Theory (TD-DFT) and Electronic Transitions.

The TD-DFT calculations can provide information about electronic transitions, which can be used for photochemical characterization. The theoretical UV-vis spectrum reveals a dominant, highly intense absorption band located within the visible region (Fig. 5). From the theoretical spectroscopic data (Table 4), the transition which occurred at 587.45 with an excitation energy of 2.1106 eV defines the dominant band as the primary absorption maximum driven mainly by the excited state 5. This state is a highly allowed and statistically probable electronic transition state with its high oscillator strength of 0.5157 release corroborate the activation mechanism.

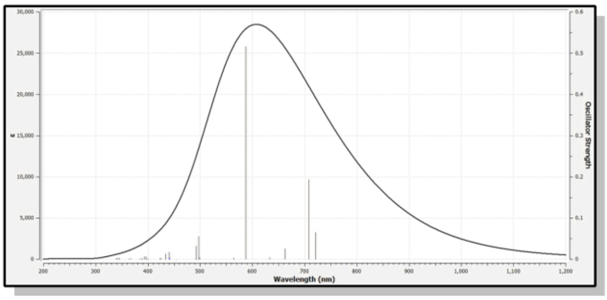

**Figure 5.** Calculated UV-Visible spectrum of $Mo(BIH)_3(CO)_3$.

The MO contributions for this excited state revealed that the strong absorption is characterized mainly by the promotion of electronic transition from HOMO -1 (MO 204) to LUMO+2 (MO 208) (Fig. 6) with a dominant expansion coefficient of 0.63401 (80.39 %). The promotion of this election triggers the metal-to-ligand charge transfer required to disrupt the M→CO backbonding. This strong absorption within the visible light region (yellow-orange light) computationally supports the viability of this substituted tricarbonyl as a PhotoCORM.

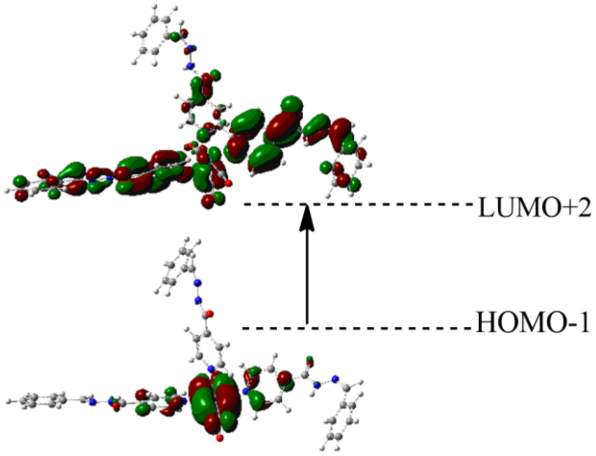

**Figure 6**. MOs showing the major electronic transition from the Mo center to the ancillary ligands, which give rise to M→L charge transfer transitions.

Its low visible light activation potentially eliminates possible phototoxicity and limits tissue penetrations associated with high energy irradiation [28-30]. This absorption led to promotion of an electron from MO204 localized on Mo to MO208 located on the extended π-system of the isonicotinic hydrazone ligand. The migration of this electron density from metal to the ancillary ligand depletes the electron used by Mo for π-backbonding with CO. The Mo-C is thereby weakened facilitating CO release. The dominant peak emerging at 570 nm in the myoglobin assay which is a proof of CO. Additional lower energy transition appearing at 707.80

**Table 3.** Theoretically calculated energy levels of the lowest-lying transitions of the tricarbonyl.

| State | Assignment | | Coefficient | Energy (eV) | Wavelength (nm) | Oscillator strength |
|---|---|---|---|---|---|---|
| | From | To | | | | |
| S0 → S1 | HOMO | LUMO | 0.6859 (94.09 %) | 1.7209 | 720.48 | 0.0645 |
| | HOMO | LUMO+2 | -0.1399 (3.91 %) | | | |
| S0 → S2 | HOMO-1 | LUMO+2 | -0.1868 (6.98 %) | 1.7517 | 707.80 | 0.1936 |
| | HOMO | LUMO+1 | 0.6579 (86.57 %) | | | |
| | HOMO | LUMO+2 | 0.1197 (2.87 %) | | | |
| S0 → S5 | HOMO-1 | LUMO | -0.1619 (5.24 %) | 2.1106 | 587.45 | 0.5157 |
| | HOMO-1 | LUMO+1 | -0.1306 (3.41 %) | | | |
| | HOMO-1 | LUMO+2 | 0.6340 (80.39 %) | | | |
| | HOMO | LUMO+1 | 0.2049 (8.40 %) | | | |

nm further extends the therapeutic optical window for the application of this compound in biological tissues by enhancing its profile for targeted phototherapy. This secondary low energy absorption is an allowed transition, primarily composed of excited State 2 (E = 1.7517 eV, f = 0.1936).

### 3.5. The CO release kinetics and delivery to deoxymyoglobin

The quantitative validation of the CO release profile of the tricarbonyl in solution was carried out via time-dependent UV-Vis spectrophotometry. A standard calibration plot of concentration against absorbance was used. Graphical plot of $\ln[\mathrm{Mo(BIH)_3CO)_3}]$ versus time yielded a linear relationship indicating CO release strictly follows first-order kinetics. By fitting of the exponentials in the first order rate equation, the apparent CO release rate (kCO) was determined to be $9.7\mathrm{x}10^{-2}$ $\mathrm{s}^{-1}$. To confirm the delivery of CO to myoglobin, the introduction of the freshly prepared solution of the carbonyl complex to the standard deoxymyoglobin assay at physiological pH (7.4), changed the initial absorption maximum at 405 nm, forming a new dominant peak at 570 nm. This shift serves as a diagnostic tool to prove the complete conversion of deoxymyoglobin to carbonmonoxy myoglobin, validating the capacity and therapeutic potential of the tricarbonyl complex to deliver CO directly to the heme centre.

### 3.6. Molecular Docking Studies

The CO release by CORM in biological systems plays well established roles. The CO release events however give rise to the generation of secondary species. These species and their actions play key roles in the successful application of the CORM. MLCT driven CO release triggers a dissociation process yielding coordinatively unsaturated metal fragments and free ligand derivatives. The careful choice of isonicotinoyl hydrazone scaffold as an ancillary ligand here is because the light-triggered release can lead to the free ligand permeating the intracellular space to interact with certain protein targets. Such interactions can enhance antibacterial, anticancer and antioxidant activities. Therefore, in silico molecular docking simulation of the hydrazone is employed to evaluate its action against selected bacterial targets and Kelch domain of Keap1 (PDB: 4L7B) for antioxidant response.

#### 3.6.1. Antibacterial

Molecular docking of the hydrazone scaffold was performed against three high-priority targets, the same as those used in experimental evaluation. The bacterial targets LasR quorum-sensing receptor of Pseudomonas aeruginosa (PDB:3IX3), PBP2a transpeptidase of Methicillin-Resistant *S. aureus* (PDB: SM18), and the DNA Gyrase B subunit of *E. coli* (PDB: 6F86) were used. The docking protocol was first validated by redocking the co-crystallized standard ligand inhibitors in the targets. The top scorer redocked ligand pose was superimposed with the proteins' co-crystallized ligands respectively. The matching of the poses showed good RMSD score of 0.95 Å, 0.54 Å, 0.99 Å, and 1.01 Å for LasR, PBP2a, DNA Gyrase and Keap1 respectively. The docking poses (Fig. 7) showed that the hydrazone remarkably conforms to the distinct active sites of both the Gram-positive and Gram-negative targets. The bonding affinity is largely driven by hydrogen bonding via the pyridine N and the hydrazone linker

#### 3.6.2. Antioxidant

Since CO is recognised to upregulate cellular antioxidant responses, it is necessary to investigate if the likely liberation of ancillary hydrazone during CO release could synergistically amplify the process. The ligand was docked against the Kelch domain of Keap1 (PDB: 4L7B), which is the primary negative regulator of the Nrf2 oxidant pathway. The result (Fig. 8) revealed the hydrazone ligand formed two stable hydrogen bonding interaction through the pyridine N with the highly conserved ARG 483, and second through the amide carbonyl oxygen with ARG 415 (2.031 Å). The hydrazone effectively fits into the shallow regulatory pocket, with a binding score of -7.068, demonstrating its likely ability to sterically inhibit the sequestration of Keap1-Nrf2 process, and potentially acting in direct synergy with the cytoprotective effect of the liberated CO.

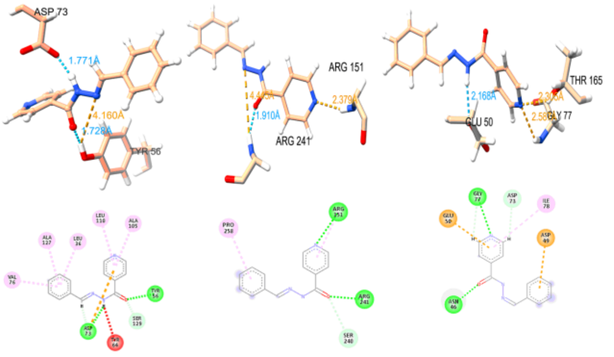

**Figure 7**. Docking pose of ancillary ligand against *P. aeruginosa* PDB: 3IX3, MRSA PDB: 5M18, and *E. coli* DNA Gyrase PDB: 6F86. The simulated interaction with MRSA (-6.119) displayed strong hydrogen bonding with ARG151 (2.379 Å) and ARG241 (1.910 Å). Similar interactions with *E. coli* DNA Gyrase (-6.646) and *P. aeruginosa* (-7.735) displayed essential hydrogen bonds with acidic residues such as ASP 73 (1.771 Å) and GLU 50 (2.168 Å), as well as stabilizing interactions with TYR 56 (1.728 Å).

These docking profiles provide theoretical evidence that, in addition to serving as a tuning moiety for the Mo core, the hydrazone ligand, upon its likely selective photo-release, may act as a broad-spectrum pharmacophore capable of disrupting essential pathogenic pathways. This synergistic activity makes the tricarbonyl complex a potentially viable photochemotherapeutic agent.

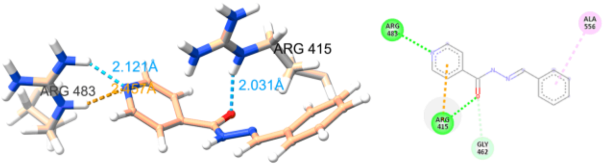

**Figure 8.** Binding interaction of the ancillary ligand with PDB: 4L7B.

### 3.7. In Vitro Antibacterial Activity

To evaluate the antibacterial potential of the complex, it was subject to in vitro susceptibility testing against *S. aureus* (Gram-positive), *E. coli* (Gram-negative), and *P. aeruginosa* (Gram-negative). The results showed potent dose-dependent zones of inhibition across all test organisms (Fig 9). The carbonyl exhibited exceptional broad-spectrum actions, yielding maximum zones of inhibition above 22 mm for the three strains. Even at the lowest concentration of 250 µM used in the evaluation, the carbonyl complex clearly outperformed the Amoxicillin control. The in vitro susceptibility of these pathogens remarkably mirrors the CO release and delivery ability of the complex, as well as the ability of the released hydrazone to halt the growth of both Gram-positive and Gram-negative bacteria. This proves that the hydrazone is a highly effective antibacterial pharmacophore that can operate synergistically alongside liberated CO.

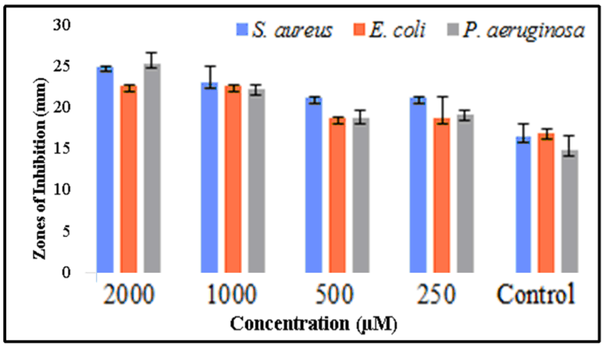

**Figure 9.** Antibacterial action of the CORM and Control against the test organisms.

## 4. Conclusion

The novel mer-$[Mo(CO)_3(BIH)_3]$ was successfully prepared by one-pot in vacuo and characterized using spectroscopic techniques. Experimental and theoretical evaluation of its potential as a synergistic, light-triggered therapeutic was carried out. Spectral analysis revealed that the nitrogen atom in the para-position of the isonicotinoylhydrazone exerts a strong electron-withdrawing effect. This weakens π-backbonding from the Mo to the carbonyl ligands and reduces the strength of the Mo-C bond, thereby rendering the complex susceptible to rapid CO release (kCO = 9.7 x $10^{-2}$ $s^{-1}$). Furthermore, TD-DFT calculations identified a robust, visible light-driven Metal-to-Ligand Charge Transfer (MLCT) transition at 587.45 nm as the primary trigger for photolysis, thereby validating the photolability of the molybdenum(0) complex.

The complex's structural design enables a dual-action therapeutic mechanism. Visible light irradiation potentially guarantees both the spatial release of cytoprotective CO and the liberation of the carefully functionalized hydrazone ancillary ligand. As validated through SwissDock modelling and in vitro assay, docking against the bacterial LasR quorum-sensing receptor of *P. aeruginosa* (PDB:31X3), PBP2a transpeptidase of MRSA (PDB: SM18), and the DNA Gyrase B subunit of *E. Coli* (PDB: 6F86), as well as Keap1 (PDB: 4L78) for antioxidant response simulation, revealed that the photo-released scaffold possesses the structural prerequisite to engage critical antimicrobial and antioxidant pathways. The in vitro testing supported the broad-spectrum action of the carbonyl. Consequently, this tricarbonyl photoCORM represents a highly promising, tunable platform for the targeted delivery of synergistic antibacterial and anti-inflammatory therapies.

## Author contributions

**Tenimu Adogah Abubakar**: Conceptualization, methodology, software, original draft. **Abdulakeem Busari**: Writing, reviewing. **Jude Ehwevwerhere Emurotu**: Resources. **Dele Peter Fapojuwo**: Formal Analysis. **Oluwagbemiga T. Amusan**: Editing. **Uche Basil Eke**: Conceptualization, Reviewing, Editing, Validation, supervision.

## Conflicts of interest

There are no conflicts to declare.

## Acknowledgement

The authors acknowledge Dr Saeed of the Center for Vaccine and Drug Development STEP-B, Federal University of Technology, Minna, Nigeria, for his support in the in vitro susceptibility evaluation.

## References

[1] C. C. Romao, "Chem Soc Rev," *Chem Soc rev*, pp. 3571–3583, 2012, doi: 10.1039/c2cs15317c.

[2] T. A. Abubakar, U. B. Eke, and D. K. Sylvestre, "S Isoniazid stabilized tungsten tricarbonyl complex: A new CO-releasing molecule with antibacterial activity," *Sci. Forum (Journal Pure Appl. Sci. J.*, vol. 19, pp. 139–144, 2019.

[3] T. A. Abubakar, U. B. Eke, and A. Salisu, "CARBON MONOXIDE RELEASING TUNGSTEN TRICARBONYL COMPLEXES WITH ANTIBACTERIAL ACTIVITY," *Bayero J. Pure Appl. Sci.*, vol. 14, no. 1, pp. 1–6, 2023, doi: http://dx.doi.org/10.4314/bajopas.v14i1.1S.

[4] S. S. Mendes *et al.*, "Synergetic Antimicrobial Activity and Mechanism of Clotrimazole- Linked CO-Releasing Molecules," *Bio Med Chem*, vol. 2, pp. 419–436, 2022, doi: 10.1021/acsbiomedchemau.2c00007.

[5] L. Flanagan, R. R. Steen, K. Saxby, and M. Klatter, "The Antimicrobial Activity of a Carbon Monoxide Releasing Molecule ( EBOR-CORM-1 ) Is Shaped by Intraspecific Variation within Pseudomonas aeruginosa Populations," *Front. Chem.*, vol. 9, no. February, pp. 1–11, 2018, doi: 10.3389/fmicb.2018.00195.

[6] M. Kubeil and H. Stephan, "Cytotoxicity of metal-containing carbon monoxide-releasing molecules : A current assessment," *J. Inorg. Biochem.*, vol. 277, no. January, 2026, doi: https://doi.org/10.1016/j.jinorgbio.2026.113235 Received.

[7] H. M. Southam *et al.*, "Carbon-Monoxide-Releasing Molecule-2 ( CORM-2 ) Is a Misnomer : Ruthenium Toxicity, Not CO Release, Accounts for Its Antimicrobial Effects," *Antioxidants*, vol. 10, no. 915, pp. 1–22, 2021, doi: https://doi.org/10.3390/antiox10060915.

[8] S. Vikrama *et al.*, "Theoretical Insights into the Mechanism of Carbon Monoxide ( CO ) Release from CO-Releasing Molecules," *Chemi Eur. J.*, pp. 1–10, 2012, doi: 10.1002/chem.201103617.

[9] N. Bauer, Z. Yuan, X. Yang, and B. Wang, "Plight of CORMs: the unreliability of four commercially available CO-releasing molecules, CORM-2, CORM-3, CORM-A1, and CORM-401, in studying CO biology," *Biochem Pharmacol.*, vol. 214, pp. 1–73,2024,doi: 10.1016/j.bcp.2023.115642.Plight.

[10] G. Frenking, I. Fern, N. Holzmann, S. Pan, I. Krossing, and M. Zhou, "Metal − CO Bonding in Mononuclear Transition Metal Carbonyl Complexes," *JACS*, vol. 1, pp. 623–645, 2021, doi: 10.1021/jacsau.1c00106.

[11] O. S. Ceren, l S. Goncagü, S. Neslihan, E. Üstün, and O. İsmail, "Synthesis, Characterization, Computational Evaluation, CO-Releasing Properties , and Molecular Docking Interactions of New [Mn(CO)3(bpy)L] PF6- Type Molecules," *ACS Omega*, vol. 10, p. 30798–30814, 2025, doi: 10.1021/acsomega.5c03085.

[12] D. Belletto, T. Shoeib, and E. Sicilia, "Photophysical Properties of a Mn (I) Tricarbonyl PhotoCORM With 8- - Aminoquinoline Ligand : Insights From Theory," *J. Comput. Chem.*, no. I, pp. 1–12, 2026, doi: 10.1002/jcc.70338.

[13] R. Seth, D. A. Jose, S. Kumar, Y. Rajneesh, and K. Ajeet, "Quest of new molecular frameworks for photoinduced carbon monoxide - releasing molecules : a computational prospective," *Theor. Chem. Acc.*, vol. 141, no. 79, pp. 1–11, 2022, doi: 10.1007/s00214-022-02937-y.

[14] R. Seth and A. Singh, "Rational design of co-ordination compounds in combination of bipyridine type of ligands and group 7 metal (M = Mn, Re) for photoCORM: a DFT study," *J. Mol. Model.*, vol. 29, no. 10, p. 306, 2023, doi: 10.1007/s00894-023-05712-3.

[15] J. Liu, H. Patrick, S. Johannes, A. H. C. Sven, K. Stephan, G. Helmar, S. Gräfe, U. Neugebauer, G. Upendar, S. Alexander, "Visible Light-Activated Biocompatible Photo-CORM for CO-release with Colorimetric and Fluorometric Dual Turn-On Response," *Polyhedron*, 2019, doi: 10.1016/j.poly.2019.04.031.

[16] V. C. Weiss *et al.*, "Luminescent PhotoCORMs: Enabling/Disabling CO Delivery upon Blue Light Irradiation," *Inorg. Chem.*, 2020, doi: 10.1021/acs.inorgchem.0c00638.

[17] A. T. Abubakar and U. B. Eke, "Trimethylamine N-oxide Promoted Decarbonylation Reactions of Molybdenum and Tungsten Hexacarbonyls with Dimethylglyoxime," *Chem. Search. J.*, vol. 8, no. 1, pp. 29–33, 2017.

[18] G. E. S. M. J. Frisch, G. W. Trucks, H. B. Schlegel *et al.*, "Gaussian 09, Revision D.01," vol. 6, no. 3, pp. 132–136, 2021.

[19] C. Ranjith and D. Ravikumar, "SwissADME predictions of pharmacokinetics and drug-likeness properties of small molecules present in Ipomoea mauritiana Jacq," *J. Pharmacogn. Phytochem.*, vol. 8, no. 5, pp. 2063–2073, 2019.

[20] D. E. V Pires, T. L. Blundell, and D. B. Ascher, "pkCSM: Predicting Small-Molecule Pharmacokinetic and Toxicity Properties Using Graph-Based Signatures," *J. Med. Chem.*, vol. 58, pp. 4066–4072, 2015, doi: 10.1021/acs.jmedchem.5b00104.

[21] S. Narramore, C. E. M. Stevenson, A. Maxwell, D. M. Lawson, and C. W. G. Fishwick, "New insights into the binding mode of pyridine-3-carboxamide inhibitors of E. coli DNA gyrase," *Bioorganic Med. Chem.*, vol. 27, no. 16, pp. 3546–3550, 2019, doi: 10.1016/j.bmc.2019.06.015.

[22] E. Jnoff, A. Claudia, J. B. John, B. Oliver, B. Edward, B. Steven, B. Frederick, B. Mark, B. Christian, C. Tom, C. Vincent, D. Graham, D. Stephanie, F. Tara, G. Christophe, E. Jigorel, J. Kwong, R. Maghames, M. Innocent, P. Richard, S. A. Zara, M. A. Smith, S. C. Christopher, C. P. Jean "Binding mode and structure-activity relationships around direct inhibitors of the Nrf2-Keap1 complex," *ChemMedChem*, vol. 9, no. 4, pp. 699–705, 2014, doi: 10.1002/cmdc.201300525.

[23] U. F. Röhrig, M. Goullieux, M. Bugnon, and V. Zoete, "Attracting Cavities 2.0: Improving the Flexibility and Robustness for Small-Molecule Docking," *J. Chem. Inf. Model.*, vol. 63, no. 12, pp. 3925–3940, 2023, doi: 10.1021/acs.jcim.3c00054.

[24] M. Bugnon *et al.*, "SwissDock 2024: major enhancements for small-molecule docking with Attracting Cavities and AutoDock Vina," *Nucleic Acids Res.*, vol. 52, no. W1, pp. W324–W332, 2024, doi: 10.1093/nar/gkae300.

[25] E. F. Pettersen *et al.*, "UCSF ChimeraX: Structure visualization for researchers, educators, and developers," *Protein Sci.*, vol. 30, no. 1, pp. 70–82, 2021, doi: 10.1002/pro.3943.

[26] E. C. Meng, D. G. Thomas, P. F. Eric, S. C. Greg, J. P. Zach, M. H. John, F. E. Thomas, "UCSF ChimeraX: Tools for structure building and analysis," *Protein Sci.*, vol. 32, no. 11, pp. 1–13, 2023, doi: 10.1002/pro.4792.

[27] B. Ercan, M. Y. Abdullah, A. Aras, F. Türkan, U. Yildiko, O. Kılıç, and A. Dey, "Dassault Systèmes BIOVIA, Discovery Studio Visualizer," *J. Food Nutr. Res.*, vol. 9, no. 3, pp. 114–123, 2021, doi: 10.12691/jfnr-9-3-3.

[28] E. Kottelat and F. Zobi, "Visible Light-Activated PhotoCORMs," *inorganics*, vol. 5, no. 24, pp. 1–19, 2017, doi: 10.3390/inorganics5020024.

[29] M. A. Wright and J. A. Wright, "PhotoCORMs : CO release moves into the visible," *Dalton Transactions*, vol. 45, pp. 6801–6811. 2016, doi.org/10.1039/CSDT04849D.

[30] I. Chakraborty, S. J. Carrington, and P. K. Mascharak, "Photodelivery of CO by Designed PhotoCORMs : Correlation between Absorption in the Visible Region and Metal – CO Bond Labilization in Carbonyl Complexes," *ChemMedChem*, vol. 9, pp. 1266–1274, 2014, doi: 10.1002/cmdc.201402007.